

ARTICLE OPEN

Optical spin locking of a solid-state qubit

J. H. Bodey¹, R. Stockill^{1,5}, E. V. Denning^{1,2}, D. A. Gangloff¹, G. Éthier-Majcher¹, D. M. Jackson¹, E. Clarke³, M. Hugues⁴, C. Le Gall^{1*} and M. Atatüre^{1*}

Quantum control of solid-state spin qubits typically involves pulses in the microwave domain, drawing from the well-developed toolbox of magnetic resonance spectroscopy. Driving a solid-state spin by optical means offers a high-speed alternative, which in the presence of limited spin coherence makes it the preferred approach for high-fidelity quantum control. Bringing the full versatility of magnetic spin resonance to the optical domain requires full phase and amplitude control of the optical fields. Here, we imprint a programmable microwave sequence onto a laser field and perform electron spin resonance in a semiconductor quantum dot via a two-photon Raman process. We show that this approach yields full SU(2) spin control with over 98% π -rotation fidelity. We then demonstrate its versatility by implementing a particular multi-axis control sequence, known as spin locking. Combined with electron-nuclear Hartmann–Hahn resonances which we also report in this work, this sequence will enable efficient coherent transfer of a quantum state from the electron spin to the mesoscopic nuclear ensemble.

npj Quantum Information (2019)5:95; <https://doi.org/10.1038/s41534-019-0206-3>

INTRODUCTION

The existence of strong electric dipole transitions enables coherent optical control of matter qubits that is both fast and local.^{1–3} The optical techniques developed to address central spin systems in solids, such as colour centres in diamond and confined spins in semiconductors, typically fall into two categories: the first makes use of ultrashort, broadband, far-detuned pulses to induce quasi-instantaneous qubit rotations in the laboratory frame.^{4–7} Achieving complete quantum control with this technique further requires precisely timed free qubit precession accompanying the optical pulses. The second technique is based on spectrally selective control via a resonantly driven two-photon Raman process,^{8–12} and allows full control exclusively through tailoring of the drive field, echoing the versatility of magnetic spin resonance. Despite this attractive flexibility, achieving high-fidelity control using the latter approach has proved challenging due to decoherence induced by the involvement of an excited state for colour centres in diamond,^{8,10,11} and due to nuclei-induced ground-state decoherence for optically active semiconductor quantum dots (QDs).⁹ In the case of QDs, the limitation of ground-state coherence can be suppressed by preparing the nuclei in a reduced-fluctuation state.^{13–17} In this Letter, we achieve high-fidelity SU(2) control on a nuclei-prepared QD spin using a tailored waveform imprinted onto an optical field. We then demonstrate the protection of a known quantum-state via an aligned-axis continuous drive, a technique known as spin locking. Finally, by tuning the effective spin-Rabi frequency, we access the electron-nuclear Hartmann–Hahn resonances, which holds promise for proxy control of nuclear states.

RESULTS

Optical electron spin resonance

Our device is an indium gallium arsenide QD, embedded in an n-type Schottky heterostructure and housed in a liquid-Helium

cryostat at 4.2 K; Fig. 1a depicts this arrangement. The QD is charged deterministically with a single electron, and a magnetic field of 3.3 T perpendicular to the growth and optical axes creates an $\omega_e = 24.5$ GHz Zeeman splitting of the electron spin states which form Λ systems with the two excited trion states. Using an electro-optic modulator (EOM), we access these Λ systems by tailoring a circularly polarised single-frequency laser, of frequency ω_L and detuned from the excited states by $\Delta_L \approx 700$ GHz. The EOM is driven by an arbitrary waveform generator (AWG) output with amplitude V_0 , frequency ω_{mw} and phase ϕ_{mw} . Operating the EOM in the regime where the microwave field linearly modulates the input optical field, a signal $V_0 \cos(\omega_{mw}t + \Delta\phi_{mw})$ produces a control field consisting of two frequencies at $\omega_L \pm \omega_{mw}$ with a relative phase-offset of $2\Delta\phi_{mw}$. This bichromatic field of amplitude Ω_L drives the two-photon Raman transitions with a Rabi coupling strength $\Omega = \Omega_L^2/\Delta_L$ between the electron spin states (see Supplementary Note 2) in the limit $(\Omega_L/\Delta_L)^2 \ll 1$. The Hamiltonian evolution is given by

$$\hat{H}_{\text{eff}} = \Omega(\cos(\phi)\hat{S}_x + \sin(\phi)\hat{S}_y) + \delta\hat{S}_z \quad (1)$$

where \hat{S}_i are the spin operators in the electron rotating frame, δ the two-photon detuning and ϕ the relative phase-offset of the Raman beams. The effect of this Hamiltonian is described geometrically by a precession of the Bloch vector around the Rabi vector $[\Omega \cos(\phi), \Omega \sin(\phi), \delta]$. We have full SU(2) control over the Rabi vector through the microwave waveform, via the Rabi frequency $\Omega \propto V_0^2$, its phase $\phi = 2\Delta\phi_{mw}$, and the two-photon detuning $\delta = \omega_e - 2\omega_{mw}$. An additional resonant optical field of 100-ns duration performs spin initialisation and readout. Finally, prior to the whole protocol, we implement the recently developed nuclear-spin narrowing scheme,¹⁷ which conveniently requires no additional laser or microwave source, in order to enhance ground-state coherence and so maximise control fidelity.

Figure 1b shows the evolution of the population of the $|\downarrow\rangle$ state for increasing durations of the Raman drive, taken at three different Raman powers. The Raman drive induces coherent Rabi

¹Cavendish Laboratory, University of Cambridge, JJ Thomson Avenue, Cambridge CB3 0HE, UK. ²Department of Photonics Engineering, Technical University of Denmark, 2800 Kgs. Lyngby, Denmark. ³EPSRC National Epitaxy Facility, University of Sheffield, Sheffield Broad Lane, S3 7HQ, UK. ⁴Université Côte d'Azur, CNRS, CRHEA, rue Bernard Gregory, 06560 Valbonne, France; ⁵Present address: Kavli Institute of Nanoscience, Delft University of Technology, Lorentzweg 1, 2628 CJ Delft, The Netherlands. *email: cl538@cam.ac.uk; ma424@cam.ac.uk

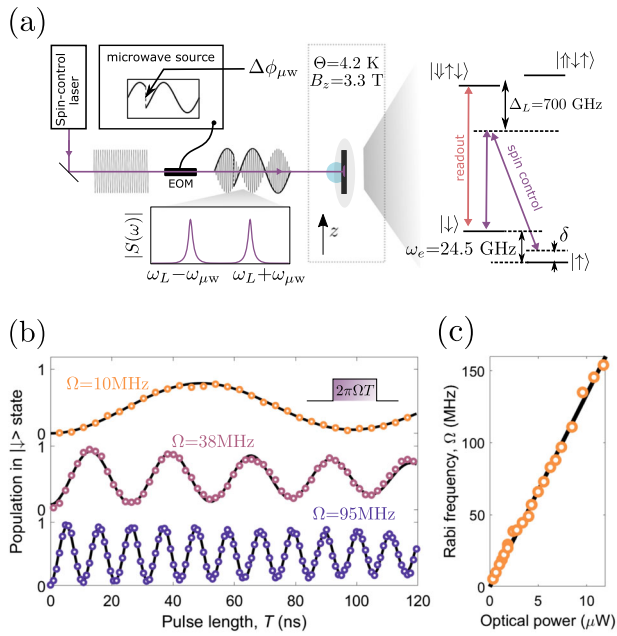


Fig. 1 All optical ESR of a QD electron spin. **a** Experimental schematic: Intensity modulation of a single-frequency laser produces two sidebands for spin-control. Encoding a phase shift $\Delta\phi_{\mu\text{W}}$ in the microwave signal produces a change of relative phase $\phi = 2\Delta\phi_{\mu\text{W}}$ between the two sidebands. These then drive two-photon Raman transitions between the energy levels of a negatively charged QD, as shown on the right. The optical fields have a single-photon detuning from the excited state of $\Delta_L \approx 700$ GHz, and a two-photon detuning from the ESR of δ . A resonant laser pulse is used to initialise the spin via optical pumping prior to spin control and to read out the population of the $|\downarrow\rangle$ state after spin control. **b** Time evolution of $|\downarrow\rangle$ -state population after drive time T taken at three different Rabi frequencies. The solid curves are fits from a Bloch-equation model to extract the Rabi frequency Ω . **c** Dependence of the Rabi frequency Ω on the laser power incident on the cryostat window. The black line is a linear fit, with a slope of $13.4 \text{ MHz} \cdot \mu\text{W}^{-1}$

oscillations within the ground-state manifold. The dependence of the fitted Rabi frequency on power is linear within the power range experimentally available as shown in Fig. 1c. This linearity is the result of modest optical power ($\sim 10 \mu\text{W}$) and a sufficiently large single-photon detuning $\Delta_L \approx 700$ GHz, allowing us to work in the adiabatic limit where excited-state population is negligible during the rotations. Even in this limit, we reach Rabi frequencies up to 154 MHz, exceeding that achieved by extrinsic spin–electric coupling^{18,19} and two orders of magnitude faster than direct magnetic control of gate-defined spin qubits.²⁰ While rotations driven by ultrafast (few ps), modelocked-laser pulses naturally circumvent ground-state dephasing, the high visibility of the Rabi oscillations achieved here suggests that our electron spin resonance (ESR) yields equally coherent rotations with the added spectral selectivity and flexibility of microwave control.

Coherence of optical rotations

We characterise the coherence of the rotations with the quality factor Q , which measures the number of π rotations before the Rabi-oscillation visibility falls below $1/e$ of its initial value. Figure 2a summarises the dependence of the Q factor and decay of the Rabi envelope on the ESR drive strength Ω and sheds light on three distinct regimes, which are dominated by one of three competing decoherence processes included in the model curve of Fig. 2: (i) inhomogeneous broadening of variance $\sigma = 4.8$ MHz, (ii) electron-mediated nuclear spin-flipping transitions arising from

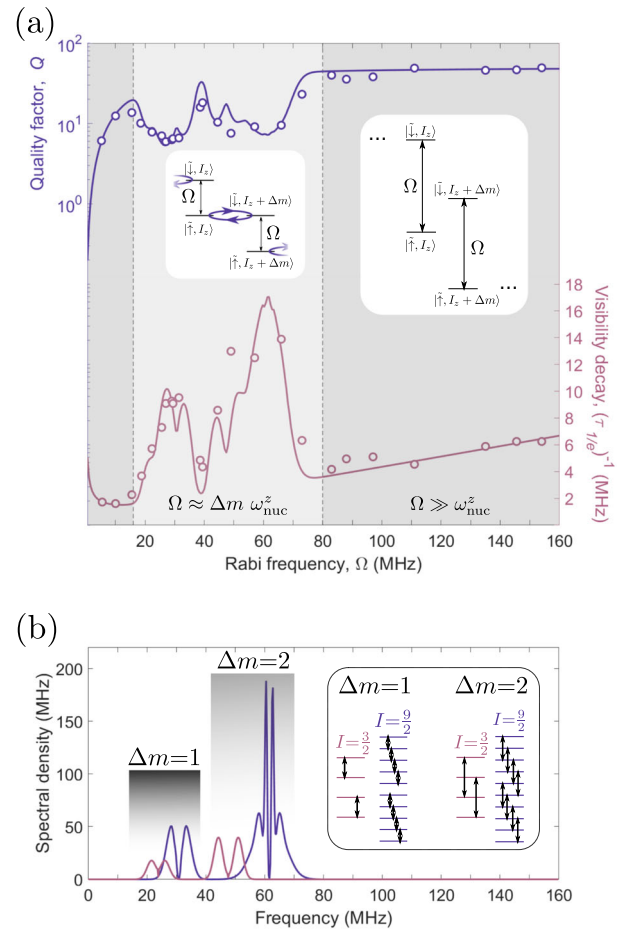


Fig. 2 ESR properties of the driven central spin. **a** Q factor of the Rabi oscillations (purple) and inverse $1/e$ -decay time of the Rabi oscillation visibility (pink) as a function of Rabi frequency. We define the visibility by taking the maximum and minimum of the Rabi curve, over a π -period. Hartmann–Hahn resonances between electron–nuclear states at $\Omega \approx \omega_{\text{nuc}}^z$ and $\Omega \approx 2\omega_{\text{nuc}}^z$ depicted in the inset emerge as an accelerated decay. **b** Calculated nuclear spectral density for Indium ($I = 9/2$) and Arsenic ($I = 3/2$). The inset indicates the transitions $\Delta m = 1$ and $\Delta m = 2$ considered in our model, which are strain-allowed to first order. In the intermediate-power regime where $\Omega \approx \Delta m \omega_{\text{nuc}}^z$, $(\tau_{1/e})^{-1}$ is equal up to a factor 2π to this density of states, after convolution with the width of the ESR transition (see Supplementary Note 4)

the presence of strain, and (iii) a spin decay proportional to the laser power, which for simplicity we cast as $\Gamma_1 = \alpha|\Omega|$ with $\alpha = 2.7 \times 10^{-2}$. In the low-power regime, where $\Omega < 18$ MHz, the fidelity is affected by nuclei-induced shot-to-shot detuning errors, which in our model are fixed according to an independent Ramsey measurement. This inhomogeneous broadening induces a non-exponential decay of Rabi oscillation visibility³ (see also Supplementary Note 3). We shield the system from this effect by increasing the Rabi frequency, yielding an increase in Q factor. The intermediate-power regime, where $\Omega = 18 - 80$ MHz, exhibits a dramatic decrease in Q and increase in decay rate. In this regime, the coherent spectrally selective drive induces electron-mediated nuclear spin-flips through a Hartmann–Hahn resonance,²¹ as we depict in the inset to Fig. 2a. Splitting the dressed electron states $|\uparrow\rangle, |\downarrow\rangle$ by an energy $\hbar\Omega$ causes the dressed electron–nuclear states to become degenerate, removing the energy cost associated to a single nuclear spin-flip $\sim \hbar\omega_{\text{nuc}}^z$. The presence of intrinsic strain, which perturbs the nuclear quantisation axis set by the external magnetic field, allows coupling between these now-

degenerate states. The decay of electronic coherence is related to the nuclear spectral density shown in Fig. 2b, which captures the strength of the strain-enabled nuclear transitions over a nuclear ensemble of $N \approx 74,000$ nuclei inhomogeneously broadened by variation of the local strain fields across the QD (see Supplementary Note 4). As an intuitive semi-classical picture, one can think of the Knight field—the electron-spin polarisation (S_z) felt by the nuclei—acting as an effective radio-frequency field of frequency Ω along the external magnetic field. Strain, tilted from this external field, is a perturbation that allows this Knight field to induce single-nucleus transitions between the eigenstates \tilde{m} and \tilde{m}' to first order (inset of Fig. 2b) provided Ω is close to ω_{nuc}^z or $2\omega_{\text{nuc}}^z$. In the high-power regime ($\Omega > 80$ MHz), we decouple from both inhomogeneous nuclear-spin fluctuations and Hartmann–Hahn transitions, and consequently observe the highest Q factors ($Q = 47.6 \pm 1.7$ over the four highest Rabi frequencies). Here, the decay envelope is dominated by Γ_1 , an optically induced relaxation between the electron states proportional to power, and independent of the single-photon detuning Δ (see Supplementary Note 3). The non-resonant and non-radiative nature of this process is consistent with electron-spin relaxation induced by photo-activated charges appearing in our device as Stark shifts of the resonance at the highest Raman power. This mechanism, extrinsic to the QD, will vary depending on device structure^{22,23} and quality. This process causes an exponential decay of the Rabi oscillations, bounding the Q factor to $4/(3\alpha)$ and the π -rotation fidelity to $f_\pi = \frac{1}{2} \times (1 + e^{-1/Q})$ (see Supplementary Note 3). Our model allows us to evaluate the non-Markovian corrections caused by the nuclear inhomogeneities and Hartmann–Hahn resonances within the spectral width $1/t_\pi = 2\Omega$ of the π pulse. At $\Omega = 154$ MHz, a correction of -0.001 applied to the experimentally measured Q factor yields a π -pulse fidelity $f_\pi = 0.9886(4)$.

Multi-axis control

Figure 3a shows Rabi oscillations taken while varying the detuning δ . With increasing $|\delta|$, the frequency of the Rabi oscillations $\Omega' = \sqrt{\Omega^2 + \delta^2}$ increases, while the amplitude Ω^2/Ω'^2 decreases, as the spin precession follows smaller circles on the Bloch sphere. This confirms that we control the polar angle θ of the Rabi vector through detuning of the microwave field. At the high Rabi frequencies used for taking these data (Fig. 3a), we observe that the Rabi drive weakly perturbs the nuclear-spin polarisation, causing detuning fluctuations which become more visible as the pulse length increases.

In Fig. 3b, we demonstrate control over the azimuthal angle of the rotation axis by stepping the phase ϕ between two consecutive $\frac{\pi}{2}$ rotations. The $|\downarrow\rangle$ -state population evolves sinusoidally with the phase shift between the two $\frac{\pi}{2}$ pulses. For example, at $\phi = 0$, the two rotations add resulting in a π rotation and maximum readout signal, whilst for $\phi = \pi$, the two pulses exactly cancel, returning the electron spin to its starting state and giving a minimum readout signal. Defining the measurement as the $(\frac{\pi}{2})_\phi$ pulse combined with the $|\downarrow\rangle$ -state readout, the phase dependence shown here demonstrates our ability to perform $S_{\pm x}$ and $S_{\pm y}$ measurements, corresponding to two-axis tomography.

Figure 3c displays Ramsey interferometry performed in the rotating frame, which allows us to further characterise our ESR control. We create a spin superposition using a resonant $\frac{\pi}{2}$ pulse that evolves for a time τ before measuring the state using a second $\frac{\pi}{2}$ pulse with a relative phase $\phi = 0$ ($\phi = \pi$), performing an S_y (S_{-y}) measurement. Within this observation window, there are no oscillations modulating the dephasing-induced decay (T_2^*), confirming that the measurement basis is phase-locked to the rotating frame to below our resolution, set by the inhomogeneous nuclear broadening. Under these optimum nuclear-spin narrowing conditions¹⁷ (see also the section “Methods”), the spin coherence decays according to $T_2^* = 47.2 \pm 0.2$ ns; this corresponds to a

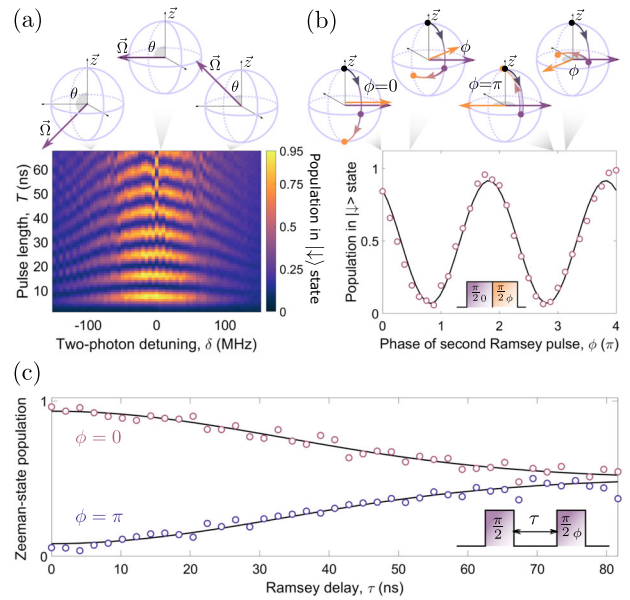


Fig. 3 SU(2) control over the rotation axis. **a** Rabi oscillations as a function of δ , at a bare Rabi frequency $\Omega = 120$ MHz. δ dictates the polar angle $\theta = \arctan(\frac{\delta}{\Omega})$ of the Rabi vector. **b** Dependence of the $|\downarrow\rangle$ -state population on the relative phase ϕ of two immediately consecutive 13 MHz $\frac{\pi}{2}$ -pulses, as $\phi_{\mu\text{w}}$ is varied between $[0, 2\pi]$. This phase corresponds to the azimuthal angle of the Rabi vector. The phase offset between maximum readout signal and constructive pulse interference is consistent with a systematic detuning of 3.5 MHz. **c** Ramsey interferometry on the electron. Two 24 MHz $\frac{\pi}{2}$ -pulses, separated by a delay τ and followed by a readout of the $|\downarrow\rangle$ ($|\uparrow\rangle$) state produce the pink (purple) data points. These data are fitted by a Gaussian envelope, $\rho(t) = \frac{\rho_0}{2} (1 \pm e^{-(t/T_2^*)^2})$ for an initial population ρ_0 , yielding a 47.4 (47.1)-ns inhomogeneous dephasing time for the upper (lower) curve

standard deviation of the spin splitting of $\sigma = 4.77 \pm 0.02$ MHz due to the hyperfine fluctuations.

An immediate opportunity derived from multi-axis control is the realisation of an optical analogue of spin locking, a magnetic resonance sequence that preserves a known quantum state well beyond its dephasing time. In this sequence (Fig. 4a), a $\frac{\pi}{2}$ rotation creates a coherent superposition state in the equatorial plane. The azimuthal angle of the rotation axis is then shifted by $\frac{\pi}{2}$, bringing the Rabi vector into alignment with the system state; this places the electron into one of the dressed states. The drive creates an energy gap $\hbar\Omega$ between the two dressed states, which provides protection against environmental dynamics occurring at frequencies different from Ω . By setting $\Omega \sim 10$ MHz, we successfully avoid nuclear-spin resonances observed in Fig. 2. In Fig. 4b we implement the spin-locking sequence for up to $0.6 \mu\text{s}$, tracking the population in the $\{|\uparrow\rangle, |\downarrow\rangle\}$ basis to give a measure of the performance of our quantum-state preservation. At these short delays, a small unlocked component of the Bloch vector undergoes Rabi oscillations resulting in small-amplitude oscillations. As confirmed with our Bloch-equation model (black curve in Fig. 4b), this arises from detuning errors of the locking pulse consistent with the measured 4.8-MHz nuclear-field inhomogeneity. The decay of the locked component of the Bloch vector is significantly slower than under a Rabi drive of the same amplitude ($\Omega = 11$ MHz) (grey model curve in Fig. 4b). Figure 4c shows the decay of the spin-locked state on longer timescales. After each locking at $\Omega = 16$ MHz, we measure the length of the Bloch vector by performing state-tomography and obtaining the visibility as in Fig. 3b. An exponential fit (black curve in Fig. 4c) reveals a decay time of $2.3 \pm 0.2 \mu\text{s}$. The close agreement with the decay rate

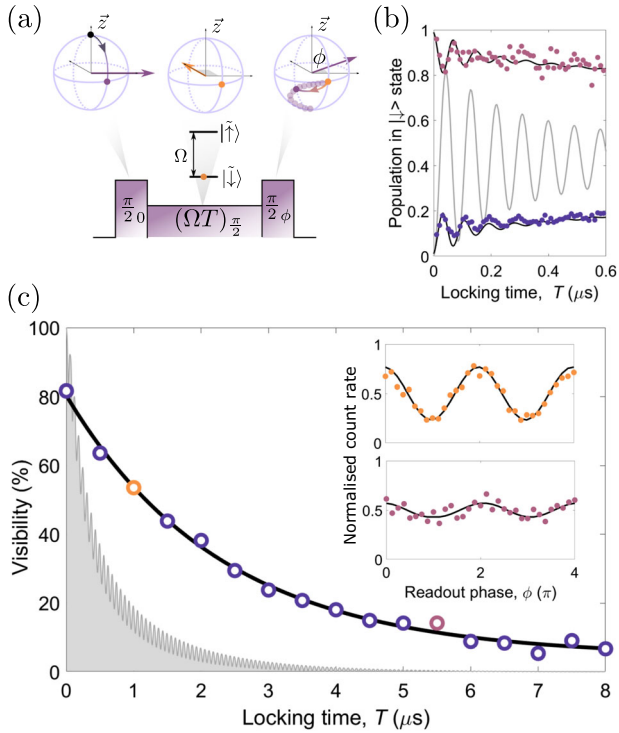


Fig. 4 Optical locking of a coherent superposition. **a** Spin-locking sequence schematic in the rotating frame. The electron, initially in the $|\uparrow\rangle_z$ state, is rotated to $|\downarrow\rangle_y = |\downarrow\rangle_x$ by the first $\pi/2$ pulse. The phase of the drive is then jumped by $\pi/2$; $|\downarrow\rangle_y$ is now an eigenstate of the drive. The system is driven in this configuration for a time T . A final $\pi/2$ pulse with phase ϕ before the $|\downarrow\rangle_z$ readout allows the equatorial spin components to be measured. **b** Spin locking with $\Omega = 11$ MHz as a function of locking time T , with a readout phase of $\phi = 0(\pi)$ producing the pink (purple) data. The data are presented alongside a Bloch-equation model (black line: spin-locking, grey line: direct Rabi drive) that accounts for the inhomogeneous broadening of $\sigma = 4.8$ MHz and spin decay Γ_1 . **c** Spin locking at $\Omega = 16$ MHz as a function of locking time T . Tomography of the state in the xy -plane is done by varying the phase ϕ of the final $\pi/2$ pulse over 4π after each locking time; the insets depict two such datasets, indicated by colour. We use these data to extract a visibility, fitted with an exponential decay time of $2.3 \pm 0.2 \mu\text{s}$ (black line). The corresponding visibility for a direct Rabi drive is plotted alongside (grey line) and exhibits decay on a 100-ns timescale. Nuclear-field inhomogeneities lead to the oscillations seen in the Rabi visibility, which is partially refocussed at integer multiples of a 2π rotation

expected from our Fig. 2 model is evidence that spin locking is similarly limited by the photo-activated spin relaxation (Γ_1). The quantum state is thus locked and preserved for a longer time than would be accessible via direct Rabi drive. This confirms our ability to implement all-optically a multi-axis spin-control sequence that can protect the qubit effectively against the intrinsic nuclear hyperfine coupling.

DISCUSSION

The high-fidelity all-optical ESR we report here enables the generation of any quantum superposition spin state on the Bloch sphere using a single waveform-tailored optical pulse. This full SU(2) control further allows the all-optical implementation of spin locking, traditionally an NMR technique, for quantum-state preservation via gapped protection from decoherence-inducing environmental dynamics. In the case of semiconductor QDs,

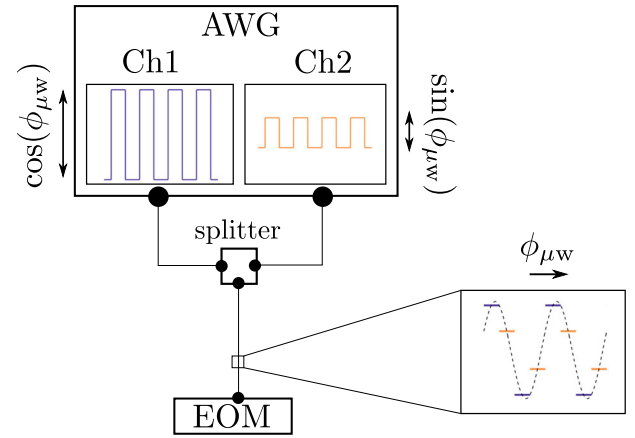


Fig. 5 Schematic of our microwave-generation apparatus. Two channels of an AWG produce square waves with an amplitude ratio of $\tan \phi_{\mu w}$. These square waves are mixed in quadrature to construct a phase-controlled sine wave, with a phase $\phi_{\mu w}$

where the nuclei form the dominant noise source, the same quantum control capability enables us to reveal directly the spectrum of nuclear-spin dynamics. An immediate extension of this work will be to perform spin locking in the spectral window of nuclear-spin resonances, i.e. the Hartmann–Hahn regime, to sculpt collective nuclear-spin states,^{24,25} and also to tailor the electron–nuclear interaction^{26–28} to realise an ancilla qubit or a local quantum register based on the collective states of the nuclear ensemble.²⁹

METHODS

Quantum dot device

Our QD device is the one used in ref. ³⁰. Self-assembled InGaAs QDs are grown by molecular beam epitaxy and integrated inside a Schottky diode structure, above a distributed Bragg reflector to maximise photon-outcoupling efficiency. There is a 35-nm tunnel barrier between the n-doped layer and the QDs, and a blocking barrier above the QD layer to prevent charge leakage. The Schottky diode structure is electrically contacted through Ohmic AuGeNi contacts to the n-doped layer and a semitransparent Ti gate (6 nm) is evaporated onto the surface of the sample. The photon collection is enhanced with a superhemispherical cubic zirconia solid immersion lens on the top Schottky contact of the device. We estimate a photon-outcoupling efficiency of 10% at the first lens for QDs with an emission wavelength around 970 nm. A home-built microscope with spectral and polarisation filtering¹⁷ is used for resonance fluorescence, with a QD-to-laser counts ratio exceeding 100:1.

Raman laser system

Sidebands are generated from the continuous-wave laser by modulating a fibre-based EOPACE EOM with a microwave derived from a Tektronix AWG 70002A. The output of the EOM depends on the voltage applied, with maximum and minimum transmissions for applied voltages V_{\max} and V_{\min} , respectively, and the π voltage of the EOM, $V_{\pi} = |V_{\max} - V_{\min}|$. Applying a voltage $V = V_{\min} + V_0(t)$, where $V_0(t)$ is a microwave field of small amplitude compared with V_{π} , the electric field at the EOM output E_{out} is described by $E_{\text{out}}(t) \propto V_0(t) \times E_{\text{in}}(t)$. In other words, we work with small amplitude around the minimum intensity transmission of the EOM to imprint the microwave amplitude onto the optical field.

Generation of the microwave signal $V_{\text{in}}(t)$ is depicted in Fig. 5. We produce a digital signal with a sampling rate that is four times the microwave frequency (a factor 2 is obtained by setting the AWG sampling rate at $2\omega_{\mu w}$ and another factor 2 is obtained by combining two independently programmable AWG outputs with a splitter). We thus arrive at a digital signal containing four bits per period, the minimum required to carry phase information to the EOM. To generate the signal shown in Fig. 5, we add the two AWG outputs in quadrature, which we

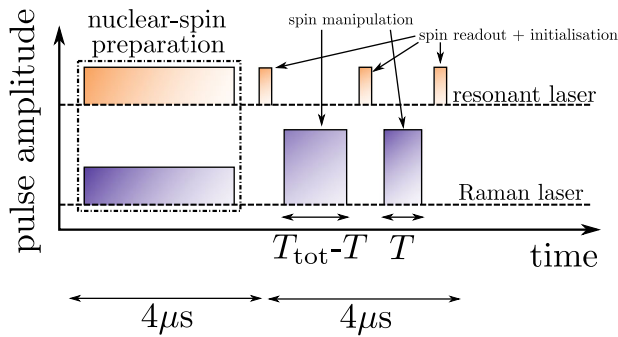


Fig. 6 A typical experimental cycle. The nuclear-spin bath is prepared using a Raman cooling technique for $4\ \mu\text{s}$, before electron spin control is performed. This takes place over a similar timescale, meaning that our duty cycle is close to 50%

realise after characterisation of the relative delay between the two microwave lines arriving at the splitter. From each output, we generate a square-wave signal at 12.25 GHz. By tuning their relative amplitudes, we construct a sinusoidal signal at 12.25 GHz whose phase ϕ is determined by the relative amplitude $A_{1,2}$ of channels 1 and 2 according to $\tan(\phi) = A_1/A_2$.

Experimental cycle

Nuclear-spin preparation. Figure 6 shows our experimental cycle which involves narrowing the nuclear-spin distribution before a spin-manipulation experiment. Nuclear-spin preparation is done using the scheme detailed in ref. ¹⁷, operating in a configuration analogous to Raman cooling in atomic systems. It involves driving the system continuously with the Raman laser, while pumping the $|\downarrow\rangle$ spin state optically. Optimum cooling, assessed using Ramsey interferometry, occurs for a Raman drive at $\Omega = 22$ MHz and a resonant repump of $\Omega_{\text{res}} = 0.9\Gamma_0/\sqrt{2}$ for an excited-state linewidth Γ_0 , in agreement with the optimum conditions found in ref. ¹⁷. These settings give an order-of-magnitude improvement in our electron spin inhomogeneous dephasing time T_2^* (Fig. 2a).

Electron spin control. During spin control, we conserve the total Raman pulse area in our sequences by pairing pulses of increasing length with pulses of decreasing length (Fig. 6). This allows us to stabilise the Raman laser power using a PID loop and maintain relative fluctuations below a per cent. We operate with a duty cycle of around 50%, preparing the nuclear-spin bath for a few μs before spending a similar amount of time performing electron spin control. The alternation on μs timescale of coherent manipulation and nuclear-spin preparation is fast compared with the nuclear-spin dynamics¹⁶ such that the nuclear-spin distribution is at steady state.

DATA AVAILABILITY

The data that support the plots within this paper and other findings of this study are available from the corresponding authors upon reasonable request.

CODE AVAILABILITY

The code used to produce the theoretical findings of this study is available from the corresponding authors upon reasonable request.

Received: 1 June 2019; Accepted: 11 September 2019;

Published online: 12 November 2019

REFERENCES

1. Arimondo, E. & Orriols, G. Nonabsorbing atomic coherences by coherent two-photon transitions in a three-level optical pumping. *Nuovo Cimento Lett.* **17**, 333–338 (1976).

2. Meekhof, D. M., Monroe, C., King, B. E., Itano, W. M. & Wineland, D. J. Generation of nonclassical motional states of a trapped atom. *Phys. Rev. Lett.* **76**, 1796–1799 (1996).
3. Johnson, T. A. et al. Rabi oscillations between ground and Rydberg states with dipole–dipole atomic interactions. *Phys. Rev. Lett.* **100**, 113003 (2008).
4. Gupta, J. A., Knobel, R., Samarth, N. & Awschalom, D. D. Ultrafast manipulation of electron spin coherence. *Science* **292**, 2458–2461 (2001).
5. Press, D., Ladd, T. D., Zhang, B. & Yamamoto, Y. Complete quantum control of a single quantum dot spin using ultrafast optical pulses. *Nature* **456**, 218–221 (2008).
6. Campbell, W. C. et al. Ultrafast gates for single atomic qubits. *Phys. Rev. Lett.* **105**, 090502 (2010).
7. Becker, J. N., Görlitz, J., Arend, C., Markham, M. & Becher, C. Ultrafast all-optical coherent control of single silicon vacancy colour centres in diamond. *Nat. Commun.* **7**, 13512 (2016).
8. Golter, D. A. & Wang, H. Optically driven Rabi oscillations and adiabatic passage of single electron spins in diamond. *Phys. Rev. Lett.* **112**, 116403 (2014).
9. Delley, Y. L. et al. Deterministic entanglement between a propagating photon and a singlet–triplet qubit in an optically active quantum dot molecule. *Phys. Rev. B* **96**, 241410 (2017).
10. Zhou, B. B. et al. Holonomic quantum control by coherent optical excitation in diamond. *Phys. Rev. Lett.* **119**, 140503 (2017).
11. Becker, J. N. et al. All-optical control of the silicon-vacancy spin in diamond at millikelvin temperatures. *Phys. Rev. Lett.* **120**, 053603 (2018).
12. Goldman, M. L., Patti, T. L., Levonian, D., Yelin, S. F. & Lukin, M. D. Optical control of a single nuclear spin in the solid state. <https://arxiv.org/abs/1808.04346> (2018).
13. Xu, X. et al. Optically controlled locking of the nuclear field via coherent dark-state spectroscopy. *Nature* **459**, 1105–1109 (2009).
14. Bluhm, H., Foletti, S., Mahalu, D., Umansky, V. & Yacoby, A. Enhancing the coherence of a spin qubit by operating it as a feedback loop that controls its nuclear spin bath. *Phys. Rev. Lett.* **105**, 216803 (2010).
15. Issler, M. et al. Nuclear spin cooling using overhauser-field selective coherent population trapping. *Phys. Rev. Lett.* **105**, 267202 (2010).
16. Éthier-Majcher, G. et al. Improving a solid-state qubit through an engineered mesoscopic environment. *Phys. Rev. Lett.* **119**, 130503 (2017).
17. Gangloff, D. et al. Quantum interface of an electron and a nuclear ensemble. *Science* **364**, 62–66 (2018).
18. Yoneda, J. et al. A quantum-dot spin qubit with coherence limited by charge noise and fidelity higher than 99.9%. *Nat. Nanotechnol.* **13**, 102–106 (2018).
19. Zajac, D. M. et al. Resonantly driven CNOT gate for electron spins. *Science* **359**, 439–442 (2018).
20. Veldhorst, M. et al. An addressable quantum dot qubit with fault-tolerant control-fidelity. *Nat. Nanotechnol.* **9**, 981–985 (2014).
21. Hartmann, S. R. & Hahn, E. L. Nuclear double resonance in the rotating frame. *Phys. Rev.* **128**, 2042–2053 (1962).
22. Houel, J. et al. Probing single-charge fluctuations at a GaAs/AlAs interface using laser spectroscopy on a nearby InGaAs quantum dot. *Phys. Rev. Lett.* **108**, 107401 (2012).
23. Ding, D. et al. Coherent optical control of a quantum-dot spin-qubit in a waveguide-based spin–photon interface. *Phys. Rev. Appl.* **11**, 031002 (2019).
24. Reynhardt, E. C. & High, G. L. Dynamic nuclear polarization of diamond. II. Nuclear orientation via electron spin-locking. *J. Chem. Phys.* **109**, 4100–4107 (1998).
25. Henstra, A. & Wenckebach, W. T. The theory of nuclear orientation via electron spin locking (NOVEL). *Mol. Phys.* **106**, 859–871 (2008).
26. Malinowski, F. K. et al. Notch filtering the nuclear environment of a spin qubit. *Nat. Nanotechnol.* **12**, 16–20 (2016).
27. Abobeih, M. H. et al. One-second coherence for a single electron spin coupled to a multi-qubit nuclear-spin environment. *Nat. Commun.* **9**, 2552 (2018).
28. Schwartz, I. et al. Robust optical polarization of nuclear spin baths using Hamiltonian engineering of nitrogen-vacancy center quantum dynamics. *Sci. Adv.* **4**, eaat8978 (2018).
29. Denning, E. V., Gangloff, D. A., Atatüre, M., Mørk, J. & Le Gall, C. Collective quantum memory activated by a driven central spin. *Phys. Rev. Lett.* **123**, 140502 (2019).
30. Stockill, R. et al. Quantum dot spin coherence governed by a strained nuclear environment. *Nat. Commun.* **7**, 12745 (2016).

ACKNOWLEDGEMENTS

This work was supported by the ERC PHOENICS grant (617985), the EPSRC Quantum Technology Hub NQIT (EP/M013243/1) and the Royal Society (RGF/EA/181068). D.A.G. acknowledges support from St John’s College Title A Fellowship. E.V.D. acknowledges funding from the Danish Council for Independent Research (Grant No. DFF-4181-00416). C.L.G. acknowledges support from a Royal Society Dorothy Hodgkin Fellowship.

AUTHOR CONTRIBUTIONS

J.H.B., R.S., D.A.G., G.É.-M., D.M.J., C.L.G. and M.A. conceived the experiments. J.H.B., R. S. and C.L.G. acquired and analysed data. E.V.D., C.L.G. and J.H.B. developed the theory and performed simulations. E.C. and M.H. grew the sample. J.H.B., R.S., E.V.D., D.A.G., G.É.-M., D.M.J., C.L.G. and M.A. prepared the manuscript.

COMPETING INTERESTS

The authors declare no competing interests.

ADDITIONAL INFORMATION

Supplementary information is available for this paper at <https://doi.org/10.1038/s41534-019-0206-3>.

Correspondence and requests for materials should be addressed to C.L.G. or M.A.

Reprints and permission information is available at <http://www.nature.com/reprints>

Publisher's note Springer Nature remains neutral with regard to jurisdictional claims in published maps and institutional affiliations.



Open Access This article is licensed under a Creative Commons Attribution 4.0 International License, which permits use, sharing, adaptation, distribution and reproduction in any medium or format, as long as you give appropriate credit to the original author(s) and the source, provide a link to the Creative Commons license, and indicate if changes were made. The images or other third party material in this article are included in the article's Creative Commons license, unless indicated otherwise in a credit line to the material. If material is not included in the article's Creative Commons license and your intended use is not permitted by statutory regulation or exceeds the permitted use, you will need to obtain permission directly from the copyright holder. To view a copy of this license, visit <http://creativecommons.org/licenses/by/4.0/>.

© The Author(s) 2019